On the Nature of Anomalously High Plasticity of High-Strength Titanium Nickelide Alloys with Shape-Memory Effects: I. Initial Structure and Mechanical Properties

V. G. Pushin[a], A. I. Lotkov[b], Yu. R. Kolobov[c], R. Z. Valiev[d], E. F. Dudarev[b], N. N. Kuranova[a], A. P. Dyupin[a], D. V. Gunderov[d], and G. P. Bakach[b]

[a] *Institute of Metal Physics, Ural Division, Russian Academy of Sciences, ul. S. Kovalevskoi 18, Ekaterinburg, 620041 Russia*

[b] *Siberian Physicotechnical Institute, Tomsk State University, pl. Novosobornaya 1, Tomsk, 634050 Russia*

[c] *Center of Nanostructured Materials and Nanotechnologies, Belgorod State University, ul. Pobedy 85, Belgorod, 308015 Russia*

[d] *Institute of Physics of Advanced Materials, Ufa State Aviation Technical University, ul. K. Marksa 12, Ufa, Bashkortostan, 450000 Russia*

Abstract—This work presents the results of studies of the $Ti_{49.4}Ni_{50.6}$ alloy of enhanced purity with shape-memory effects in an ordinary coarse-grained state with an average grain size of 20–30 μm or in a submicrocrystalline state with an average grain size of 0.2–0.3 μm. In this alloy the initial structure, phase composition, martensitic transformations, mechanical properties, and character of fracture have been investigated in a wide temperature range. It has been shown that upon cooling and mechanical tests at room temperature, the alloy exhibits highly reversible thermoelastic martensitic transformations. It has been established that the alloy exhibits high values of the strength and plastic properties and strain-hardening coefficients.

INTRODUCTION

Among the structural and functional materials that undergo martensitic transformations, the titanium nickelide alloys exhibit the highest strength and plastic properties [1–14]. Moreover, they demonstrate the effects of thermomechanical memory unique in magnitude and reproducibility, high reliability and durability of their realization (mechanothermal, mechanocyclic, and thermocyclic). With their good weldability, high corrosion resistance, biological compatibility, and comparatively simple chemical composition, they likewise are characterized by a high technological effectiveness of the metallurgical process and subsequent production conversions. As shape-memory alloys, they have no analogs and are irreplaceable in critical articles and devices of new generation in engineering and medicine [1–14].

Nowadays, there are known three main mechanisms of anelastic deformation of metallic materials, namely, by slip, twinning, and martensitic transformation. It is the anelasticity accompanied and caused by a martensitic phase transition that, manifesting itself as the third (after ordinary elasticity and plasticity) main mechanism of mechanical behavior of crystalline materials, ensures their unique features known as effects of shape memory and superelasticity. It should be noted that in the titanium nickelide alloys with highly reversible thermoelastic martensitic transformations, the observed effects of strong and isotropic softening of elasticity moduli, one-way shape memory, superelasticity, repeatedly reversible (multiple-way) shape memory, high internal friction, and damping are greatest and most widely used in practice. Along with the deformation and temperature effects, force effects of generation and relaxation of stresses upon thermoelastic martensitic transformations, both forward and reverse, are of great importance in practice [1–14].

In these alloys, depending on the technology of their synthesis, different structural states can be realized, such as single-crystal or polycrystalline (ordinary coarse-grained (CG), submicrocrystalline (SMC), or nanocrystalline (NC)) states, and single-phase or multiphase states. The method of severe plastic deformation (SPD) in combination with heat treatment is one of the most efficient methods of obtaining bulk submicrocrystalline and nanocrystalline high-strength titanium nickelide alloys [14–24]. Yet, whereas the majority of materials with submicrocrystalline and nanocrystalline structures produced by SPD possess high values of the yield strength and ultimate strength but a reduced room-temperature plasticity (relative elongation of 10–20%) [25–26], the metastable titanium nickelide alloys manifest an unusually high ability to deformation and, which is especially important, a high uniform elonga-

Table 1. Critical temperatures of the $B2 \longrightarrow B19'$ and $B2 \longrightarrow R \longrightarrow B19'$ martensitic transformations of the $Ti_{49.4}Ni_{50.6}$ alloy in the quenched state and after ECAP at 450°C ($n = 8$)

State	M_s', °C	M_f', °C	A_s', °C	A_f', °C	M_s, °C	M_f, °C	A_s, °C	A_f, °C
Quenching from 800°C	–	–	–	–	15	–5	25	35
ECAP at 450°C, $n = 8$	20	10	20	30	–20	–30	20	30

tion upon tension [3, 5, 8, 10, 11]. The complex study we undertook in this work is devoted to a comparative analysis of the mechanical behavior, structural and phase transformations upon tension, and an analysis of the nature of anomalous plasticity of metastable titanium nickelide alloys. The work consists of two parts. In the first part, we study the initial microstructure and mechanical properties of the alloys. The second part is devoted to a detailed investigation of the mechanisms of plastic deformation of these alloys and an analysis of the nature of their anomalous mechanical properties, especially plasticity.

EXPERIMENTAL

As material for the investigation, we chose the $Ti_{49.4}Ni_{50.6}$ (at %) alloy obtained from high-purity components (99.99%) by electric-arc melting in a helium atmosphere. According to the chemical-analysis data, the elemental composition of impurities in the alloy was (wt %) 0.0372 C, 0.0001 S, 0.0167 O_2, and 0.0003 N. The ingots were subjected to multiple remelting, long-term homogenizing annealing in a vacuum furnace, and repeated thermomechanical treatment, including forging into rods.

In the initial state after the final annealing at 800°C for 1 h followed by quenching in water, the alloy has an ordinary polyhedral coarse-grained (CG) structure with a most frequently occurring average grain size of 20–30 μm. To obtain the nanostructural (SMC + NC) state, the alloy rods 120 mm long and 20 mm in diameter were subjected to multiple SPD using the method of equal-channel angular pressing (ECAP) at a temperature of 450°C (angle of channel intersection $\Phi = 110°$, the number of passes $n = 8$, route B_c [15, 16]). The tests of mechanical properties for tension in a vacuum of 10^{-4} mmHg in a wide temperature range (20–600°C) at two tension rates (1×10^{-3} and 1×10^{-4} s^{-1}) were conducted on plane tensile samples with a gage base of $5 \times 2 \times 0.5$ mm. The tests at room temperature in air were also carried out on a small tensile-testing machine with a tension rate of 3×10^{-4} s^{-1} using plane minisamples with a gage base of $1 \times 1 \times 0.25$ mm and on a conventional tensile-testing machine using standard cylindrical specimens 3 mm in diameter with a gage base of 15 mm (the latter were employed to analyze the alloy microstructure depending on the degree of deformation in the cross sections transverse and longitudinal with respect to the tension axis).

The electron-microscopic investigations of the microstructure of the samples in the initial CG state, in the SMC state after ECAP, and after their mechanical tests for tension to different degrees of deformation were performed using JEM-200CX and CM-30 transmission electron microscopes at the Center of Electron Microscopy of the Institute of Metal Physics, Ural Division, Russian Academy of Sciences. The thin-foil samples were prepared on a Tenupol-5 setup. The surface relief was also studied by the method of optical metallography in situ on plane polished tensile samples in the process of tension. The phase composition of the alloy and the temperatures of the start and finish of the forward and reverse martensitic transformations were controlled in situ by the $\theta/2\theta$ method of X-ray diffraction analysis and measurements of temperature dependences of electrical resistivity ρ and magnetic susceptibility χ. The inclusions of carbides (TiC) and intermetallic oxides ($Ti_4Ni_2O_x$) that were detected by X-ray diffraction have not been found by transmission electron microscopy, which suggests that their amount does not exceed 0.2–0.3 wt %.

The critical temperatures of the start and finish of the forward (M_s, M_f) and reverse (A_s, A_f) $B2 \longrightarrow B19'$ transformations of the $Ti_{49.4}Ni_{50.6}$ alloy in the initial quenched state are listed in Table 1. These measurements were conducted by the two-tangents method from the temperature dependences of the magnetic susceptibility $\chi(T)$. The results obtained differ from the resistivity-measurement data by no more than ±3°.

RESULTS AND DISCUSSION

1. Initial Microstructure and Phase Transformations in the Alloy upon Cooling

In ordinary polycrystalline (CG) state the alloys based on the intermetallic compound TiNi exhibit a granular structure of the $B2$ austenite in which the average grain size is usually less than 100 μm and varies depending on the thermomechanical treatment used [1–14]. In the CG alloy we studied in this work, the average grain size, as was already noted, was 20–30 μm. It is known that in the titanium nickelide alloys on the threshold of martensitic transformations there appear specific pretransition states that develop as elasticity moduli experience strong isotropic softening [3, 5, 10, 27–29]. Their substructure is characterized by the presence of coherent nanodomains in which the positions of periodically displaced atoms approach those characteristic of the lattice of future martensitic phases [3, 5, 10,

11]. In the electron-microscopic images, these nanostructural states manifest themselves as specific diffraction effects (in the form of deformation-induced tweed contrast); in the electron, neutron, and X-ray diffraction patterns, in the form of diffuse effects and other specific effects such as nonradial streaks and extra reflections in positions slightly incommensurate with the reflections of the future martensitic phases R, $B19$, and $B19'$ of the $1/3\langle 110\rangle^*$ and $1/2\langle 110\rangle^*$ type. Figure 1 displays high-resolution images of tweed contrast typical of the metastable austenitic CG alloy $Ti_{49.4}Ni_{50.6}$ and electron microdiffraction patterns of two "rational" sections $(100)_{B2}$ and $(111)_{B2}$ (corresponding to the zone axes of the reflecting planes $[100]_{B2}$ and $[111]_{B2}$) with diffuse streaks and satellites of the above types.

Cooling the quenched alloy in a CG state to below the critical temperature M_s leads to the $B2 \longrightarrow B19'$ martensitic transformation. The lattice parameters of a monoclinically distorted $B19'$ phase of the $Ti_{49.4}Ni_{50.6}$ alloy are close to $a = 0.289$ nm, $b = 0.412$ nm, $c = 0.462$ nm, and $\beta = 97°$ [3–11]. We established in the X-ray diffraction experiments in situ upon cooling that the volume changes upon this transformation have a negative value $\Delta V/V = -(0.03–0.04)\%$ at the transition point, whereas the linear distortions are anisotropic (for example, they are negative along the axes of orientation relationships (ORs) $[100]_{B2} \parallel [100]_{B19'}$ and $[01\bar{1}]_{B2} \parallel [010]_{B19'}$ and positive along the axes of the $[011]_{B2} \parallel [001]_{B19'}$ OR) and gradually increase in absolute value upon cooling. With a well-known variety of the morphological variants of the $B19'$ martensite [10, 11], it is the multipacket morphology of platelet microcrystals which are twinned in pairs according to the corresponding crystallographic systems of ORs that is the main morphological variant below the finish temperature of the forward transformation M_f (Fig. 2). The linear sizes of coherent packets are, as a rule, close to 2–3 μm. Up to 1000 packets are formed in grains with sizes of 20–30 μm. As follows from the dark-field electron microscopy and trace analysis, the microcrystals themselves contain secondary plane nanotwins along the $(11\bar{1})$ and $(001)_{B19'}$ planes. In certain selected-area electron diffraction patterns (for example, close to the zone axis of the former $B2$-phase [111], see Fig. 2), they are associated with sharp streaks along $[11\bar{1}]^*$ and $[001]^*$. The $B2 \longrightarrow B19'$ transformation is realized completely, and

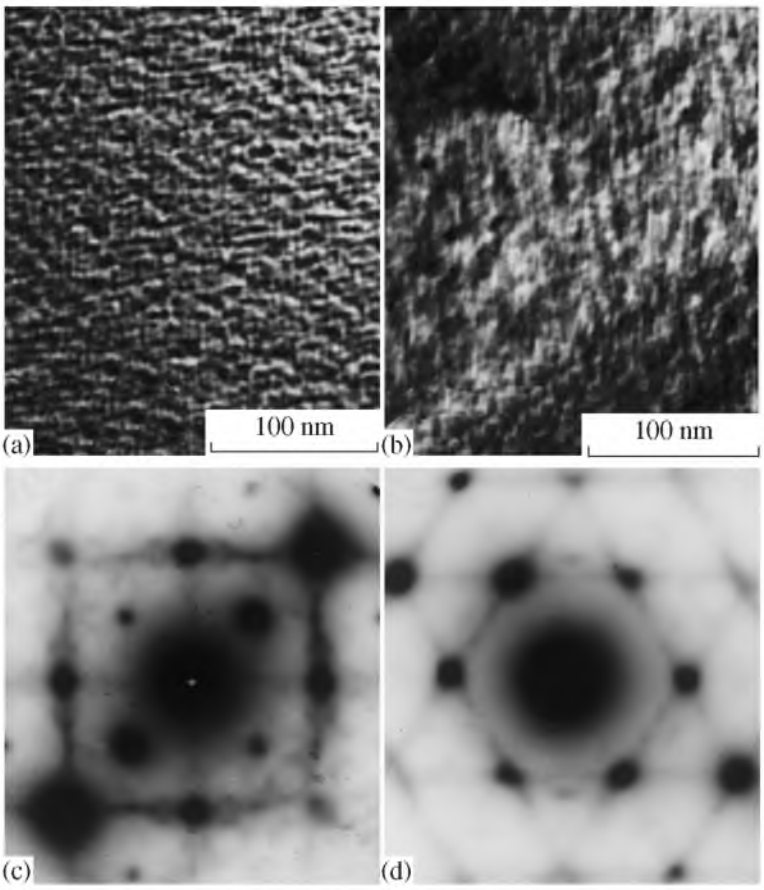

Fig. 1. (a, b) Typical electron-microscopic images of the tweed contrast and (c, d) the corresponding SAED patterns of the $Ti_{49.4}Ni_{50.6}$ alloy in the pretransition austenitic state ((c) zone axis [100] of the $B2$ phase; (d) zone axis [111]).

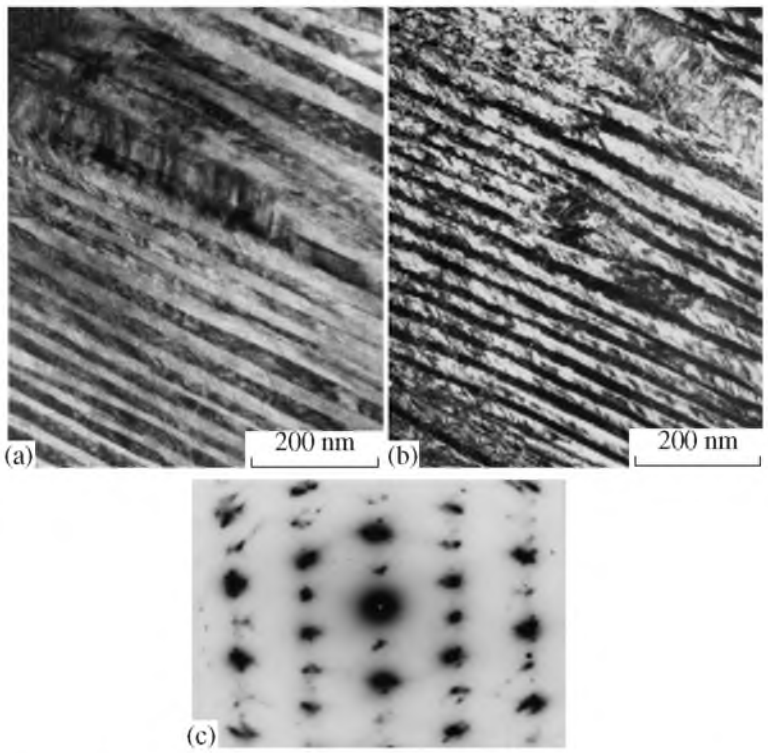

Fig. 2. (a) Bright-field and (b) dark-field electron-microscopic images and (c) an SAED pattern (zone axis [$1\bar{1}0$] of the $B19'$ phase) of a finely twinned packet $B19'$ martensite of the $Ti_{49.4}Ni_{50.6}$ alloy.

below the M_f temperature the alloy does not virtually contain retained austenite.

If this quenched alloy is subjected to low-temperature tempering or thermocycling through the temperature interval of the $B2 \longleftrightarrow B19'$ martensitic transformation or if the alloy is cooled with a furnace from 800°C, instead of quenching in water, then the formation of the $B19'$ martensite in it is accompanied by the $B2 \longrightarrow R$ transition in the initial or retained austenite. Upon cooling to below the start temperature of the $B2 \longrightarrow R$ transition (M_s'), there initially appear thin platelike crystals of the R martensite with the $\{110\}_{B2}$ habit, which arise homogeneously in the bulk of grains and heterogeneously at structural defects (dislocations, boundaries and subboundaries, second-phase inclusions) [3, 5, 10, 11]. In the rhombohedral setting, the lattice parameters of the R phase are close to a_R = 0.90 nm and α_R = 89.5°–89.0°; in the hexagonal setting, they are close to a_H = 0.734 nm and c_H = 0.528 nm [3, 5, 8, 10, 11]. It is important that at the point of the $B2 \longrightarrow R$ transition the change in the specific volume $\Delta V/V$ is small and negative and its value is –0.01 to –0.02%, whereas the changes in the lattice parameters of the R phase and, correspondingly, the linear distortions along and across the axis of the rhombohedral expansion $\langle 111 \rangle_{B2}$ are anisotropic and upon cooling become greater in absolute value by two orders of magnitude ($\Delta c/c \approx 1.0\%$, $\Delta a/a \approx -1.0\%$) [10, 11]. For this reason, after the completion of the $B2 \longrightarrow R$ transition, in the alloy there are present coherent packets of R crystals that are twinned in pairs on different habit and twinning planes $\{110\}_{B2}$ and $\{100\}_{B2}$ (Fig. 3). As a rule, their linear dimensions do not exceed several micrometers. The variants of the $\{100\}_{B2}$ twinning are usually encountered at interpacket junctions, which can be both wavy and serrated (see Fig. 3) [10, 11]. Cooling results in the following $R \longrightarrow B19'$ transformation (in Fig. 3 the $B19'$ martensite is seen on the right). Then, upon further cooling, the alloy becomes completely single-phase and acquires the $B19'$ structure which is virtually analogous to that illustrated in Fig. 2 for the quenched alloy.

It is evident that the structure-morphological hierarchy arising in the titanium nickelide alloys upon the $B2 \longrightarrow B19'$, $B2 \longrightarrow R$, and $B2 \longrightarrow R \longrightarrow B19'$ martensitic transitions is a result of a spatial self-organization of martensite crystals due to the elastic (coherent) self-accommodation of anisotropic stresses caused by thermoelastic martensitic transformations and has various spatial levels, e.g., nano (nanotwins), micro (microcrystals), meso (packet-pyramidal morphologies within a grain), and macro (the whole multipacket polycrystalline macroobject). As is known, changes in the external and internal conditions (temperature, pressure, stresses and deformations, grain size, etc.) either initiate adap-

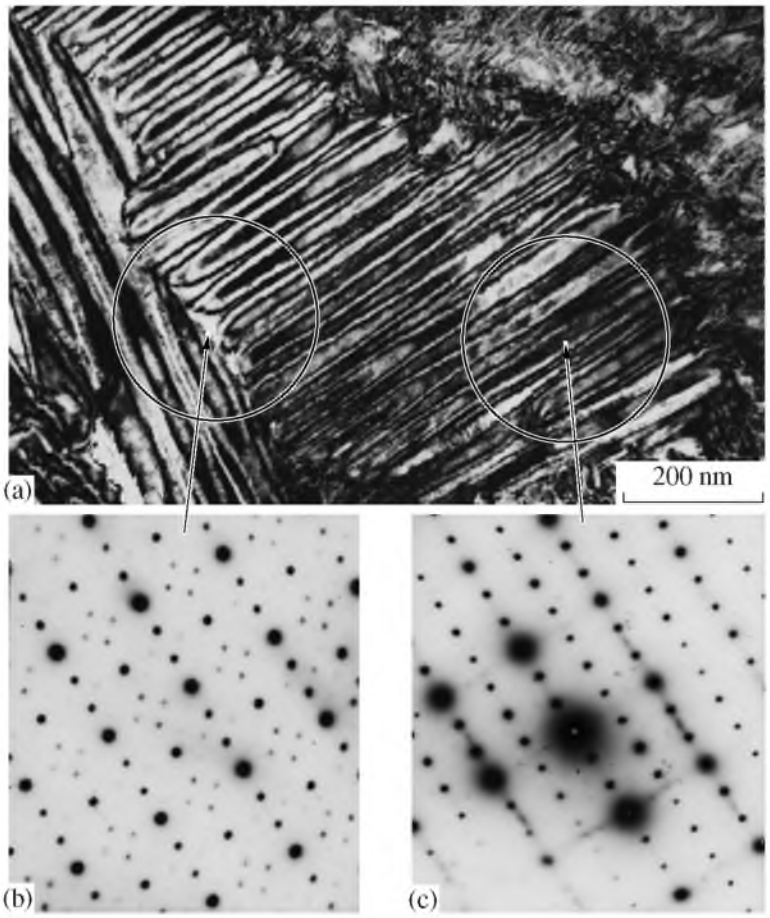

Fig. 3. (a) A bright-field electron-microscopic image and (b, c) SAED patterns (zone axis [100] of the former $B2$ phase, ((b) on the left and (c) on the right) of packets of the R martensite of the $Ti_{49.4}Ni_{50.6}$ alloy in a two-phase ($R + B19'$) state.

tive processes in this hierarchic multilevel system of elastically stressed crystals or eliminate it altogether.

The ECAP technology makes it possible to subject metals and alloys to severe plastic deformation without changes in the cross section of workpieces, which, in turn, makes it possible to repeatedly deform them and to obtain a nanostructural state in them [25, 26]. In the case of difficultly deformable intermetallic compounds, to which titanium nickelide can be referred, the ECAP was performed at elevated temperatures (350–500°C) [14–24]. In these works, bulk nanostructured alloys based on titanium nickelide, which possess extremely high values of strength and other mechanical properties, were obtained for the first time, and their structure, phase transformations, physicomechanical properties, and parameters of the ECAP process were investigated. In this study, the nanostructural state in the $Ti_{49.4}Ni_{50.6}$ alloy was attained by using ECAP at 450°C in 8 passes.

Typical electron-micrographs and selected-area diffraction (SAED) patterns obtained from transverse and longitudinal cross sections of the $Ti_{49.4}Ni_{50.6}$ alloy after ECAP are shown in Fig. 4. At room temperature this alloy also is in the austenitic $B2$ state and has a mixed grain–subgrain SMC structure with predominance of high-angle boundaries, which leads to a ringlike arrangement of reflections in the electron diffraction patterns (see Fig. 4c). The average size of grains/subgrains is close to 0.30 μm with the spread of the most frequently encountered sizes from 0.1 to 0.55 μm. In the transverse section, the SMC structure looks as equiaxed; in the longitudinal cross section (along the ECAP axis), some prolateness of individual SMC grains (with a small anisotropy factor of 1.5–2) is observed. A crystallographic texture also takes place; this is clearly seen in the SAED pattern shown in Fig. 4c; in particular, the $(200)_{B2}$-type reflections are substantially less intense and occur markedly more rarely. The presence of an enhanced density of dislocations that are comparatively uniformly distributed over all grains and subgrains is characteristic of the intragrain substructure of the SMC alloy after ECAP. The circumstance that in typical micrographs presented in Fig. 4 the images of many grains are completely free of dislocation contrast or have a very low dislocation density is a spurious result. Systematic investigations with the use of inclination of the samples in the microscope goniometer made it possible to obtain in each of available SMC and NC grains

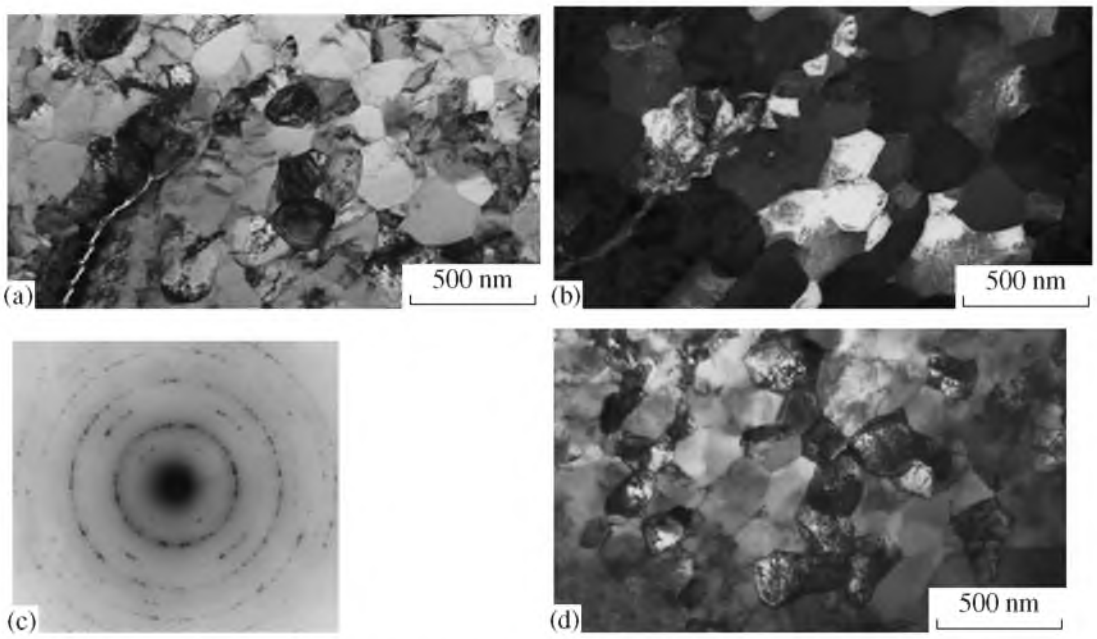

Fig. 4. (a, d) Typical bright-field and (b) dark-field electron-microscopic images and (c) an SAED pattern of the $Ti_{49.4}Ni_{50.6}$ alloy after ECAP at 450°C, $n = 8$; (a, b, c) transverse sections and (d) longitudinal cross section.

and subgrains images of the dislocation substructure of the same density as in the neighboring grains with initially visible dislocations or, on the contrary, to "extinguish" the contrast from these dislocations.

It was established that upon cooling the SMC $Ti_{49.4}Ni_{50.6}$ alloy obtained by ECAP undergoes sequential $B2 \longrightarrow R \longrightarrow B19'$ martensitic transformations. In this case, the temperatures of the forward $B2(R) \longrightarrow B19'$ transition are reduced by 30–40 K, demonstrating a stabilizing effect of a decrease in the grain size on this martensitic transformation. The critical temperatures of the $B2 \longleftrightarrow R$ (primed) transition, on the contrary, somewhat increase, and this transformation begins to go ahead of the $B19'$-martensite formation (see Table 1). As the electron-microscopic experiments in situ (upon cooling in the microscope column) showed, the dominant morphology of the R and $B19'$ martensites in SMC grains is single-packet and pairwise twinned (Figs. 5, 6). According to the trace analysis, the habit of the platelike martensite crystals in neighboring SMC grains is oriented at large angles (30°–90°), indicating the adaptive accommodation nature of this micromorphology in neighboring SMC grains. It was found that in this case the secondary internal nanotwins in the $B19'$ martensite are mainly composite accomodation nanotwins of the $(001)_{B19'}$ type. The $(11\bar{1})_{B19'}$-type twins typical of the CG state are encountered quite rarely. It is important to note here that we succeeded in revealing fine features of the microstructure of the R and $B19'$ martensites by using different-sized diaphragms of an objective lens with an image diameter of 1 and 0.3 μm. This ensured the appearance of both "Debye" rings of composite electron diffraction patterns (see Figs. 5c, 6c) and pointlike single-crystal patterns (Figs. 5d, 6d).

2. Mechanical Behavior of the Alloy at Room Temperature

As was already noted, the deformation behavior of the $Ti_{49.4}Ni_{50.6}$ alloy in the CG and SMC states was stud-

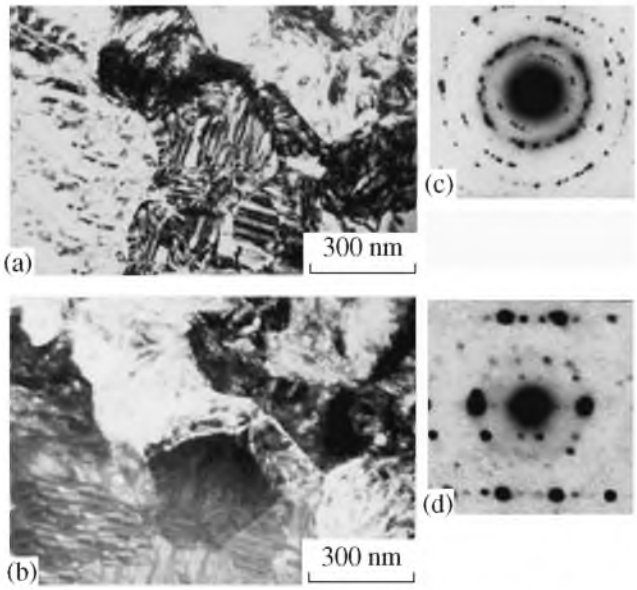

Fig. 5. (a) Bright-field and (b) dark-field electron-microscopic images of the R martensite and (c, d) SAED patterns of the ECAP-treated $Ti_{49.4}Ni_{50.6}$ alloy; the SAED patterns were obtained in situ at 0°C using (c) a large diaphragm with a diameter of 1.0 μm and (d) a small diaphragm with a diameter of 0.3 μm.

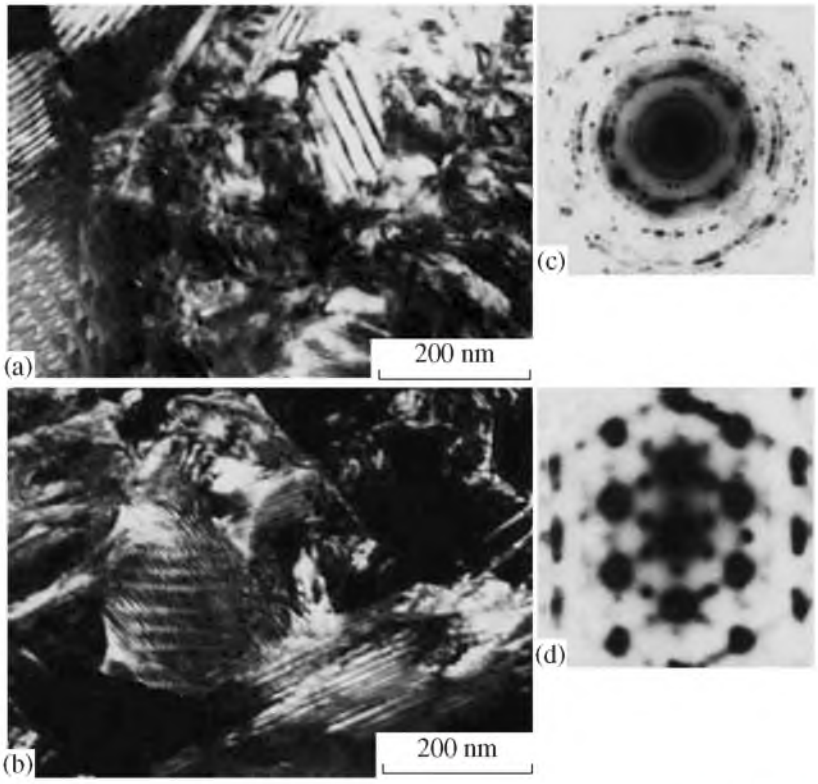

Fig. 6. (a) Bright-field and (b) dark-field electron-microscopic images of the *B*19' martensite and (c, d) SAED patterns of the ECAP-treated $Ti_{49.4}Ni_{50.6}$ alloy; the SAED patterns were obtained in situ at –100°C using (c) a large diaphragm with a diameter of 1.0 μm and (d) a small diaphragm with a diameter of 0.3 μm.

ied upon tension at rates of 1×10^{-4} and 1×10^{-3} s^{-1}. The room-temperature tests were conducted on different testing machines with the use of plane and cylindrical specimens. In doing so, the true stress σ was calculated on the assumption that in the process of tension the samples experienced uniform deformation ($\sigma = P_\varepsilon/S_\varepsilon$, $S_\varepsilon = S_0/(1 + \varepsilon)$), and that the relative deformation is $\varepsilon = (l - l_0)/l_0$; where P_ε is the force of the tensile-testing machine at the degree of deformation ε, l_0 and l are the initial and the current sample lengths, and S_0 is the initial cross section. Figure 7 displays typical true-stress–relative-deformation (σ–ε") curves upon tension in the premartensitic state (at room temperature); curve *1* corresponds to the alloy with a CG structure (after quenching); curve *2*, to the alloy with an SMC structure (after ECAP). The strength and plastic characteristics obtained are listed in Table 2.

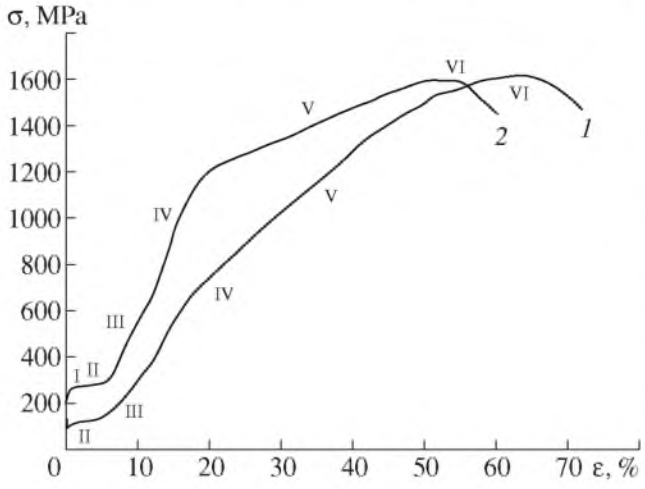

Fig. 7. The tensile true-stress–relative-deformation curves for the $Ti_{49.4}Ni_{50.6}$ alloy with (*1*) CG and (*2*) SMC structure at 20°C.

The investigations performed showed that, irrespective of the strain rate and the sample size, almost the same qualitative changes in the mechanical properties and type of the σ–ε tensile curves are observed in the alloy upon transition from the coarse-grained to the submicrocrystalline structure. Before the onset of plastic deformation, as long as the deformation is a consequence of martensitic transformation, the alloy with the submicrocrystalline structure shows the same regularities of strain hardening as those characteristic of the initial state with a coarse-grained structure. Before the attainment of the dislocation yield strength σ_y, the alloy in both structural states exhibits four stages in the σ–ε curves (stages I, II, III, and IV in Fig. 7), which differ in the magnitude of the hardening coefficient $K = \frac{d\sigma}{d\varepsilon}$ and the character of its change with an increase

Table 2. Strength and plastic characteristics of the $Ti_{49.4}Ni_{50.6}$ alloy in the CG and SMC states upon tension at room temperature

State	σ_m, MPa	σ_y, MPa	σ_u, MPa	ψ, %	δ, %	δ_u, %	K_{III}, MPa	K_{IV}, MPa	K_V, MPa
CG	130	600	1630	62	72	63	3200	6600	3000
SMC	260	1180	1600	68	60	53	6000	11500	1500

in the degree of deformation. The stage I (of elastic deformation of the *B*2 austenite) is characterized by a high hardening coefficient K_I which decreases sharply with increasing degree of deformation (transition to stage II with a so called plateau of phase pseudoyield caused by mechanically induced martensitic transformation) with a relative elongation of up to ~5%. By analogy with plastic deformation, it is common practice to call the stress of its onset as the phase pseudo-yield stress σ_m. At subsequent two stages (III and IV)—up to the dislocation yield strength σ_y—strong strain hardening is observed.

It is natural that the more than a hundredfold decrease in grain size upon ECAP substantially affects the levels of mechanical properties of the alloy under study. The stresses of the onset of all the stages, including stage V of plastic deformation, and the hardening coefficients K_{III} and K_{IV} are substantially greater in the case of SMC structure than for the alloy with a CG structure. Thus, the phase (σ_m) and dislocation (σ_y) yield stresses and the hardening coefficients K_{III} and K_{IV} after ECAP are twice as high as in the initial coarse-grained state.

The physical nature of the multistage development of anelastic martensitic deformation will be considered in [30] (in press). Yet, at this point, some additional unusual properties of the deformation behavior of the alloy with an SMC structure upon plastic deformation in the process of testing (see Fig. 7, curve *2*) should be noted. First, in the σ–ε curve after reaching the yield stress σ_y there exists a linear stage of strain hardening of the same length as for the alloy in the coarse-grained state. Second, for the SMC alloy the yield stress σ_y is twice as large whereas its hardening coefficient K_V, on the contrary, is half as large. Third, in the coarse-grained alloy the linear $\sigma(\varepsilon)$ dependence is replaced by the parabolic dependence as early as at the stage of uniform deformation, whereas in the SMC alloy the linear $\sigma(\varepsilon)$ dependence is retained almost up to the ultimate strength σ_u. Fourth, when employing our ECAP regime we can, at the same magnitude of the ultimate strength, significantly enhance the yield stress and simultaneously to retain the unusually high values of the relative elongation and reduction of area of the alloy (see Table 2).

At the final stage of mechanical tests, when the alloy reaches the ultimate strength in the both structural states, the macrolocalization of plastic deformation (stage VI in Fig. 7) observed in the form of a neck begins. In this case, in the engineering tensile curves there occurs a "drop" in the magnitude of the offset yield stress up to failure of the samples, which is also retained for the recalculated curves. In the framework of the calculation method chosen, we calculated true stresses only to values not exceeding σ_u, since the transition to the localized deformation (necking) cannot be strictly taken into account through the relative elongation. The length of stage VI in the tensile curves characterizes the localized elongation $\delta_{loc} = \delta - \delta_u \approx 7$–$9\%$.

3. Mechanical Behavior of the Alloy at Elevated Temperatures

The tensile curves and, correspondingly, mechanical characteristics of the $Ti_{49.4}Ni_{50.6}$ alloy measured at elevated test temperatures are presented in Figs. 8 and 9 and in Table 3. Unlike room temperature, at temperatures of 200°C (curves *2*) and higher (400°C, curves *3*; 500°C, curves *4*; 600°C, curve *5*), the deformation of the alloy in the state of stable austenite in the process of test already is not able to initiate martensitic transformation, and the type of the tensile curves changes radically. It is natural that at these temperatures no stages II–IV related to the development of a mechanically induced anelastic martensitic deformation are present in the σ–ε curves for the alloy in both structural states (CG and SMC). The applied stresses σ initially increase linearly (stage I). At stresses higher than σ_y, the stage of the linear $\sigma(\varepsilon)$ dependence is absent, and only the stage of a parabolic $\sigma(\varepsilon)$ dependence is observed, with a hardening coefficient $d\sigma/d\varepsilon$ which decreases continu-

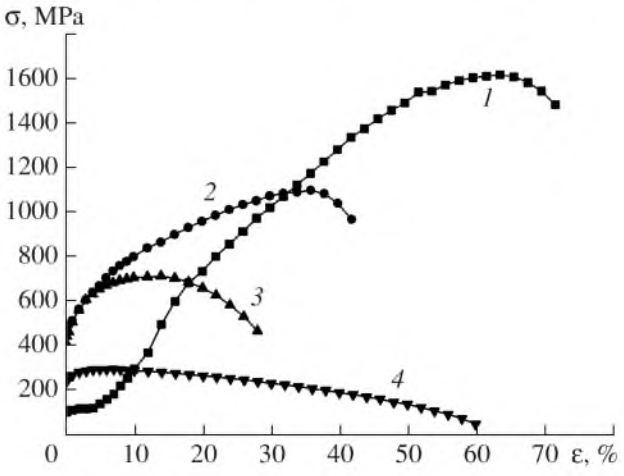

Fig. 8. The tensile true-stress–relative-deformation curves for the $Ti_{49.4}Ni_{50.6}$ alloy in the CG state; test temperatures: (*1*) 20, (*2*) 200, (*3*) 400, and (*4*) 500°C.

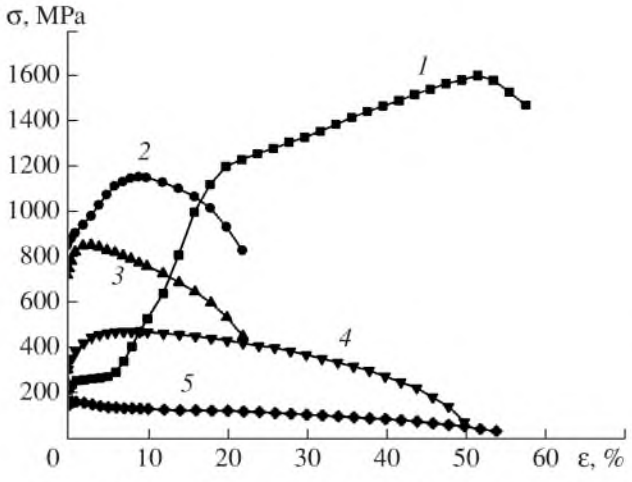

Fig. 9. The tensile true-stress–relative-deformation curves of the $Ti_{49.4}Ni_{50.6}$ alloy in the SMC state; test temperatures: (*1*) 20, (*2*) 200, (*3*) 400, (*4*) 500, and (*5*) 600°C.

ously as the degree of deformation grows (stage V). Stage VI is connected, as usually, with the onset of the macrolocalization of plastic deformation (necking). The samples always experience failure in the region of the neck.

When the test temperature rises (above 200°C), along with a decrease in the strength characteristics and a sharp drop in the uniform plastic deformation δ_u, the relative reduction of area (Ψ) in the neck grows. The relative elongation at fracture (δ) changes not quite monotonically; first, it decreases and then increases.

The strengthening attained due to the SMC-state formation is retained at elevated test temperatures; at temperatures of up to 500°C, the yield stress of the SMC alloy is higher than that of the CG alloy by a factor of 1.5–2 (see Table 3).

In both structural states (coarse-grained and submicrocrystalline), the alloy exhibits a normal strain-rate dependence of the yield stress, which increases with a temperature rise. At all temperatures in the range of 20–600°C, the yield stress grows with increasing strain rate.

4. Character of Fracture of the Alloy upon Tension

The alloy in the coarse-grained and submicrocrystalline states upon tension at rates of 1×10^{-3} and 1×10^{-4} s^{-1} at room temperature experiences failure after a sufficiently large plastic deformation; i.e., the fracture in it is ductile in terms of deformation. At the same time, the fracture in both states is brittle transcrystalline in terms of surface structure. No difference in the character of fracture of the samples in the coarse-grained and submicrocrystalline states was revealed. No secondary cracks on the fracture surface are present; in many places, different-sized dimples arising as a result of the breakaway of oxide particles ($Ti_4Ni_2O_x$) present in the alloy are observed. Some fracture elements are nearly equiaxed in shape, whereas the others have a nonequiaxed shape, and the size of these fracture elements is much the same in both structural states of the alloy. The average size of the equiaxed fracture elements is approximately 3–4 μm, and the anisotropy coefficient for the elongated fracture elements is 2–8.

When the temperature of deformation increases to 200°C, the character of fracture in terms of deformation remains unaltered (ductile) but changes substantially in terms of structure; it becomes ductile–brittle in both structural states. No secondary cracks are found, as in the room-temperature case. On the fracture surface, both equiaxed and nonequiaxed dimples are observed, and their size ranges from 0.25 to 2.5 μm. The character of fracture at 400°C is the same as at 200°C; the size of dimples on the fracture surface remains virtually unaltered and no secondary cracks on the fracture surface are seen; only the fraction of ductile fracture has increased.

The character of fracture markedly changed as the temperature of deformation increased to 500–600°C, when the degree of plastic deformation in the neck increased still further. In terms of structure, the fracture became ductile with a typical dimple relief. The area occupied by dimples on the fracture surface exceeded

Table 3. Strength and plastic characteristics of the $Ti_{49.4}Ni_{50.6}$ alloy in the CG and SMC states at different test temperature

State	Test temperature, °C	σ_m, MPa	σ_y, MPa	σ_u, MPa	ψ, %	δ, %	δ_u, %
CG	20	130	600	1630	62	72	63
	200	–	500	1100	56	42	30
	400	–	440	700	67	30	9
	500	–	240	300	94	60	5
SMC	20	260	1160	1600	68	58	51
	200	–	860	1180	73	22	10
	400	–	720	880	84	22	4
	500	–	320	500	93	51	8
	600	–	140	180	95	54	2

50%. The size of dimples sharply increased, and they acquired an equiaxed shape. The size of the largest dimples reached 8 μm.

Thus, it turned out that the effect of the deformation temperature on the character of fracture in terms of deformation and structure is practically independent of the structural state; the effect is virtually the same in the coarse-grained and submicrocrystalline states. Moreover, no significant difference in the size of typical fracture fragments between these states of the alloy is revealed.

CONCLUSIONS

In this work, the initial structure and mechanical properties of the metastable $Ti_{49.4}Ni_{50.6}$ alloy with shape-memory effects and superelasticity were investigated. The alloy has an enhanced purity in the carbon and oxygen impurities; it contains less than 0.3 wt % carbide (TiC) inclusions and intermetallic ($Ti_4Ni_2O_x$) phases. The alloy in the initial quenched coarse-grained state with an average grain size of 20–30 μm undergoes a highly reversible $B2 \longrightarrow B19'$ transformation both upon cooling to below 15°C and upon deformation under the conditions of mechanical tests by uniaxial tension at room temperature. Upon the mechanical tests, it was established that this alloy demonstrates high values of the ultimate strength (σ_u = 1630 MPa) and plasticity (ψ = 62%, δ = 72%).

In the alloy subjected to equal-channel angular pressing, its grained structure became refined by a factor of 100 (to 0.2–0.3 μm), the martensitic-transformation sequence upon cooling was changed to the $B2 \longrightarrow R \longrightarrow B19'$ with a decrease in the temperature of the second transition $R \longrightarrow B19'$ to –20°C, and the dislocation yield stress σ_y increased from an initial 600 MPa to 1180 MPa upon the retention of the other high mechanical characteristics (σ_u = 1600 MPa, ψ = 68%, δ = 60%). Both states (coarse-grained and submicrocrystalline) of the alloy are characterized by extremely high values of the uniform elongation and reduction of area (δ_u = 63 and 53%, respectively).

The mechanisms of plastic deformation and the nature of the anomalously high plasticity will be considered in the second part of this work ([30], in press).

ACKNOWLEDGMENTS

This work was supported in part by the Russian Foundation for Basic Research, project nos. 05-02-16728 and 05-08-33381; the International Science and Technology Center, project no. 3208; the Complex Integration Project of Siberian Branch and Ural Division of the Russian Academy of Sciences; a Program no. 3.6.2 of Fundamental Research of the Siberian Branch of the Russian Academy of Sciences, project no. 3.6.2.2; and the State Contracts nos. 02.513.11.3053 and 02.513.11.3197.

REFERENCES

1. I. I. Kornilov, O. K. Belousov, and E. V. Kachur, *Titanium Nickelide and Other Alloys with Memory Effect* (Nauka, Moscow, 1977) [in Russian].
2. V. A. Likhachev, S. P. Kuz'min, and Z. P. Kamentseva, *Shape Memory Effect* (Izd-vo Leningrad. Univ., Leningrad, 1987) [in Russian].
3. V. N. Khachin, V. G. Pushin, and V. V. Kondrat'ev, *Titanium Nickelide: Structure and Properties* (Nauka, Moscow, 1992) [in Russian].
4. *Materials with Shape Memory Effect*, Ed. by V. A. Likhachev (SPbGU, St. Petersburg, 1998) [in Russian].
5. V. G. Pushin, V. V. Kondrat'ev, and V. N. Khachin, *Pretransition Effects and Martensitic Transformations* (Ural. Otd. Ross. Akad. Nauk, Ekaterinburg, 1998) [in Russian].
6. V. E. Gyunter, G. Ts. Dambaev, P. G. Sysolyatin, et al., *Medical Materials and Implants with Shape Memory*, (Izd-vo Tomsk. Univ., Tomsk, 1998) [in Russian].
7. *Shape Memory Materials*, Ed. by K. Otsuka and C. V. Wayman (Cambridge University Press, Cambridge, 1998).
8. V. N. Zhuravlev and V. G. Pushin, *Alloys with Thermomechanical Memory and Their Application in Medicine* (Ural. Otd. Ross. Akad. Nauk, Ekaterinburg, 2000) [in Russian].
9. *Shape Memory Alloys: Fundamentals, Modeling and Application*, Ed. by V. Brailovski, S. Prokoshkin, P. Terriault and F. Trochu (Ecole de technologie superieure (ETS), Université du Québec, Montreal, 2003).
10. V. G. Pushin, S. D. Prokoshkin, R. Z. Valiev, et al., *Titanium Nickelide Alloys with Shape Memory Effect: Part. I. Structure, Phase Transformations, and Properties* (Ural. Otd. Ross. Akad. Nauk, Ekaterinburg, 2006) [in Russian].
11. V. G. Pushin, "Alloys with a Thermomechanical Memory: Structure, Properties, and Application," Phys. Met. Metallogr. **90** (Suppl. 1), S68–S95 (2000).
12. S. D. Prokoshkin, V. G. Pushin, E. P. Ryklina, and I. Yu. Khmelevskaya, "Application of Titanium Nickelide-Based Alloys in Medicine," Phys. Met. Metallogr. **97** (Suppl 1), S56–S96 (2004).
13. K. Otsuka and X. Ren, "Physical Metallurgy of Ti–Ni–Based Shape Memory Alloys," Prog. Mater. Sci. **50**, 511–678 (2005).
14. V. Brailovski, I. Yu. Khemelevskaya, S. D. Prokoshkin, et al., "Foundation of Heat and Thermomechanical Treatments and Their Effect on the Structure and Properties of Titanium Nickelide-Based Alloys," Phys. Met. Metallogr. **97** (Suppl. 1), S3–S55 (2004).
15. V. G. Pushin, V. V. Stolyarov, R. Z. Valiev, et al., "Features of Structure and Phase Transformations in Shape Memory Ti–Ni-Based Alloys after Severe Plastic Deformation," Ann. Chim.-Sci. Mater. **27** (3), 77–88 (2002).
16. V. G. Pushin, V. V. Stolyarov, R. Z. Valiev, et al., "Development of Methods of Severe Plastic Deformation for the Production of High-Strength Alloys Based on Titanium Nickelide with a Shape Memory Effect," Phys. Met. Metallography **94** (Suppl 1), S54–S68 (2002).
17. V. G. Pushin, R. Z. Valiev, and L. I. Yurchenko, "Processing of Nanostructured TiNi Shape Memory Alloys:

Methods, Structures, Properties, Application," J. Phys. IV France **112**, 659–662 (2003).

18. V. G. Pushin and R. Z. Valiev, "The Nanostructured TiNi Shape Memory Alloys: New Properties and Applications," Solid State Phenom. **94**, 12–21 (2003).
19. V. G. Pushin, "Structures, Properties, and Application of Nanostructured Shape Memory TiNi-Based Alloys," in *Nanomaterials by Severe Plastic Deformation*, Ed. by M. Zehetbauer and R. Valiev (Wiley–VCH, Weinheim, 2004), pp. 822–828.
20. V. N. Grishkov, A. I. Lotkov, E. F. Dudarev, et al., "Martensitic Transformations in Nanostructured TiNi-Based Alloys Produced by Severe Deformation via Rolling," Fiz. Mezomekh. **7** (Special Issue, Part 2), 26–29 (2004).
21. E. F. Dudarev, G. P. Bakach, Yu. R. Kolobov, et al., "Localization of Martensitic Deformation at Meso- and Macro-Scale Levels in Coarse-Grained and Submicrocrystalline Alloys with Shape Memory Effect," Fiz. Mezomekh. **7** (Special Issue, Part 1), 127–130 (2004).
22. V. V. Stolyarov, E. A. Prokof'ev, S. D. Prokoshkin, et al., "Structural Features, Mechanical Properties, and the Shape-Memory Effect in TiNi Alloys Subjected to Equal-Channel Angular Pressing," Fiz. Met. Metalloved. **100** (6), 91–102 (2005) [Phys. Met. Metallogr. **100** (6), 608–618 (2005)].
23. V. G. Pushin, R. Z. Valiev, Y. T. Zhu, et al., "Effect of Equal Channel Angular Pressing and Repeated Rolling on Structure, Phase Transformations and Properties of TiNi Shape Memory Alloys," Mater. Sci. Forum **503–504**, 539–544 (2006).
24. V. G. Pushin, R. Z. Valiev, Y. T. Zhu, et al., "Effect of Severe Plastic Deformation on the Behavior of Ti–Ni Shape Memory Alloys," Mater. Trans. JIM **47** (03), 694–697 (2006).
25. R. Z. Valiev and I. V. Aleksandrov, *Nanostructured Materials Produced by Severe Plastic Deformation* (Logos, Moscow, 2000) [in Russian].
26. Yu. R. Kolobov, R. Z. Valiev, G. P. Grabovetskaya, et al., *Grain-Boundary Diffusion and Properties of Nanostructured Materials* (Nauka, Novosibirsk, 2004) [in Russian].
27. A. I. Lotkov and A. V. Kuznetsov, "Elastic Properties of Ti–Ni Single Crystals before $B2 \longrightarrow B19'$ and $B2 \longrightarrow R \longrightarrow B19'$ Martensitic Transformations," Fiz. Met. Metalloved. **66** (5), 903–909 (1988).
28. V. N. Grishkov, A. I. Lotkov, S. F. Dubinin, et al., "Modulation of Short-Wavelength Atomic Displacements Preceding the $B2 \longrightarrow B19'$ Martensitic Transformation in a TiNi-Based Alloy," Fiz. Tverd. Tela **46** (8), 1348–1354 (2004)[Phys. Solid State **46** (8), 1386–1393 (2004)].
29. V. N. Grishkov, S. F. Dubinin, A. I. Lotkov, et al., "Displacive Superstructure that Precedes the $B2 \longrightarrow B19'$ Martensitic Transformation in a Titanium Nickelide-Based Alloy," Fiz. Met. Metalloved. **99** (4), 101–112 (2005) [Phys. Met. Metallogr. **99** (4), 435–446 (2005)].
30. E. F. Dudarev, R. Z. Valiev, Yu. R. Kolobov, et al., "Nature of the Abnormally High Plasticity of High-Strength NiTi Alloys with Shape Memory Effects: Plastic-Deformation Mechanisms upon Isothermal Loading," Fiz. Met. Metalloved. [Phys. Met. Metallogr.] (in press).